



UNIVERSITY OF LEEDS

This is a repository copy of *An Inductorless Direct-injection Power Control Circuit for the Distribution Grid*.

White Rose Research Online URL for this paper:

<https://eprints.whiterose.ac.uk/211225/>

Version: Accepted Version

Proceedings Paper:

Lu, M., Fan, Y. orcid.org/0000-0001-8038-7337, Zhang, C. et al. (1 more author) (2023) An Inductorless Direct-injection Power Control Circuit for the Distribution Grid. In: 2023 IEEE Energy Conversion Congress and Exposition (ECCE). 2023 IEEE Energy Conversion Congress and Exposition (ECCE), 29 Oct - 02 Nov 2023, Nashville, TN, USA. IEEE , pp. 6279-6283. ISBN 9798350316445

<https://doi.org/10.1109/ecce53617.2023.10362491>

© 2023 IEEE. Personal use of this material is permitted. Permission from IEEE must be obtained for all other uses, in any current or future media, including reprinting/republishing this material for advertising or promotional purposes, creating new collective works, for resale or redistribution to servers or lists, or reuse of any copyrighted component of this work in other works.

Reuse

Items deposited in White Rose Research Online are protected by copyright, with all rights reserved unless indicated otherwise. They may be downloaded and/or printed for private study, or other acts as permitted by national copyright laws. The publisher or other rights holders may allow further reproduction and re-use of the full text version. This is indicated by the licence information on the White Rose Research Online record for the item.

Takedown

If you consider content in White Rose Research Online to be in breach of UK law, please notify us by emailing eprints@whiterose.ac.uk including the URL of the record and the reason for the withdrawal request.



eprints@whiterose.ac.uk
<https://eprints.whiterose.ac.uk/>

An Inductorless Direct-injection Power Control Circuit for the Distribution Grid

Mowei Lu¹; Yejing Fan²; Chunxu Zhang³; Stefan M. Goetz¹

¹Department of Engineering, University of Cambridge, Cambridge, United Kingdom, ml2010@cam.ac.uk, smg84@cam.ac.uk

²School of Electronic and Electrical Engineering, University of Leeds, Leeds, United Kingdom, el17yf@leeds.ac.uk

³School of Electrical Engineering and Automation, Harbin Institute of Technology, Harbin, China, 21s006083@stu.hit.edu.cn

Abstract—This paper presents an inductorless direct-injection power flow and quality control topology. The circuit removes any bulky low-frequency transformer and includes a shunt active front end and high-frequency links that powers a series floating module per phase. These floating modules are connected in series with each phase and omit any ground connection, thereby only dealing with a small portion of the voltage difference. Unlike other low-voltage power controllers with full converters, the direct-injection circuit presented here does not need to handle full power, which allows for the utilization of low-voltage high-current GaN transistors. As a result, high-frequency switching can be adopted, and the conventional filtering inductor in series can be replaced by parasitic inductance naturally occurring between cables. Overall, the circuit is exceptionally small and compact by employing low-power components and omitting line transformers and inductors.

Index Terms—distribution grids, low-voltage grids, power flow, power quality

I. INTRODUCTION

Recent advances in renewable energy distributed generation have brought up power flow problems in the low-voltage grid. Power levels of electric vehicle (EV) chargers, previously seen only in entire villages, can rapidly fluctuate, and wide photovoltaic (PV) installations on roofs also contribute to the array of largely uncontrolled sources in the distribution network [1]–[3]. The presence of PV and EV chargers in distribution networks can potentially cause power flow reversals and reactive power disturbances [4]. These additional sources in the grid can result in uncontrolled power flows in the event of another grid segment’s failure. It’s critical to have effective strategies to manage and rectify power flow between two grids. This suggests a growing need for more focus on power flow control in the distribution grid, especially within low-voltage power systems.

Nonetheless, the distribution grid currently leans heavily on traditional mechanical or passive elements, such as switched shunt capacitor banks or on-load tap changers. These can only adjust the voltage of the entire feeder but lack the flexibility to control the power flow [5]. In high-voltage scenarios, the unified power flow controller (UPFC) is the most frequently used flexible AC transmission system device that can regulate the voltage, modify line impedance, and shift the phase either simultaneously or selectively [6]. It consists of two voltage source converters, both connected to

the same dc link and attached to the transmission line via transformers, with one connected in series and the other in parallel. The same topology is also used in low-voltage grids but is referred to as the unified power quality conditioner (UPQC) [8], primarily addressing power quality issues such as current/voltage imbalances, voltage flicker, voltage swell/sag, and current/voltage harmonics.

Although circuits based on the UPFC structure have been used for the distribution grid recently for power flow problems, known as SOPs (soft open points) or energy routers [5], [7], they tend to couple to the grid through bulky low-frequency transformers, which are heavy and expensive. More importantly, it suffers from magnetic loss and low bandwidth, especially at high frequency [9], [13]. The other type of low-voltage power flow control circuit is the back-to-back converter, which connects in series with two feeders directly, without the need for a line-frequency transformer. However, the devices have to withstand full voltage and full current [10].

The topology proposed in this paper can merge the UPFC/UPQC functions and omits any grid-connected series or parallel low-frequency transformers, thereby enhancing power density and compactness. It utilizes high-voltage low-current devices at the shunt side and low-voltage high-current devices at the series side, which offers particular advantages for the low-voltage distribution grid. Additionally, the direct injection circuit can employ the recently developed low-voltage high-current Gallium Nitride (GaN) transistors. GaN has notable benefits compared to traditional Silicon (Si) devices, including zero recovery loss, minimal capacitive core loss, short rise/fall time, and good parallel capability. Consequently, high-frequency switching can be adopted to significantly minimize the series filtering inductors. Even the parasitic inductance formed in the utility cabinet, where our circuit is installed, suffices the requirement.

II. CIRCUIT TOPOLOGY

A. System Overview

The system configuration depicted in Fig. 1 includes a low-current power supply that operates at full voltage and features a shunt active front end (AFE), as well as an isolated dc/dc converter for each phase. This configuration shifts the supply power to higher frequencies to achieve a more compact design

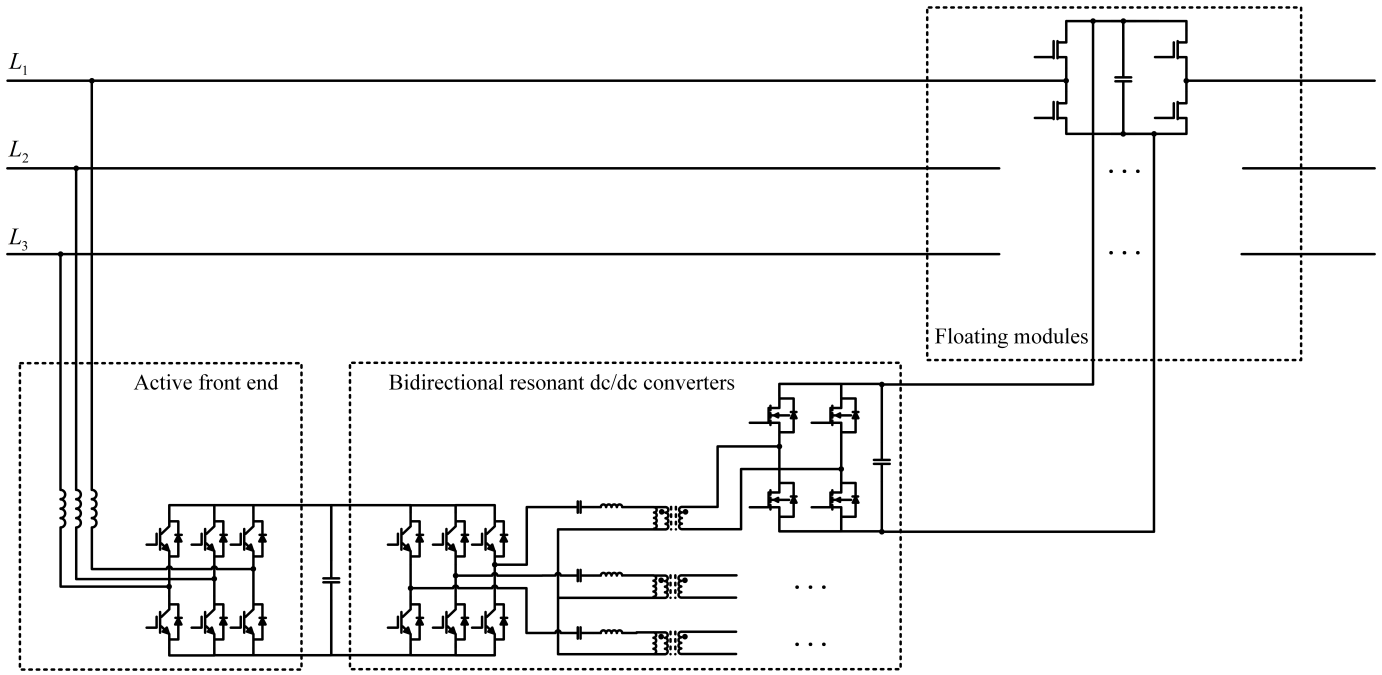


Fig. 1. Circuit configuration of the DI-UPF/QC

and less magnetic material for isolation while also incorporating a floating high-current, low-voltage series module. The design is built upon our previous work on modular floating, low-voltage high-current, and high-voltage low-current circuits [11], [12]. By taking advantage of advancements in power semiconductors, which have been driven by the consumer electronics, appliances, and automotive industries, this proposed design of a full-voltage low-current supply and low-voltage high-current modules that float with the line potential can achieve significant power density and dynamics.

Our centerpiece floating modules follow the electrical potential of their designated phases without grounding or linking to any other phases and can maintain a low local voltage, e.g., below 48 V for low-voltage grids. Consequently, we can use low-voltage transistors and capacitors. Moreover, ultra-high-speed switching power devices such as Gallium Nitride High Electron Mobility Transistors (GaN-HEMT) can be used to further reduce the filtering inductors. The GS61008 with a voltage rating of 100 V, a current rating of 90 A, and the ability to switch up to 10 MHz would be an ideal choice. If high-frequency switching leads to larger EMI, ferrite cores can be implemented for suppression.

B. Floating module control

The AFE can follow the well-established PWM rectifiers' control method and provide a constant dc output [14]. This voltage can be stepped down by the isolated dc/dc converter to supply the floating module. Since both the series side and the shunt side of the circuit are controlled in a closed-loop manner, the high-frequency dc/dc stage can employ open-loop control.

The series modules possess three switching states: a bypass state that enables current to flow around the floating dc-link capacitor and injects no voltage, along with two series states possessing positive and negative polarities. These states momentarily link the floating dc-link capacitor between the grid terminals on the left and right (Fig. 2). A continuous bypass mode also deactivates flow control. In this situation, the entire system is bypassed, and the grid functions without conditioning. Given that the latest low-voltage transistors can handle currents even at low-voltage-grid short-circuit levels, this mode could additionally function as a safe state during system failures.

While operating under flow control, each module introduces a low amplitude AC voltage across its own terminals, modulating via bypass and series modes. For example, when a module bridges two grid sectors or feeders with varying voltages and exactly preserves this voltage difference, no current passes through. Conversely, if the voltage is either smaller or larger, active current begins to flow, causing the series module to either extract or inject energy into its DC link. The module also has the capability to compensate for any phase difference between the connected grid segments.

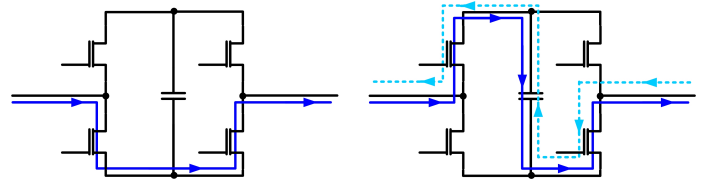


Fig. 2. Working modes: bypass state (left); serie (right).

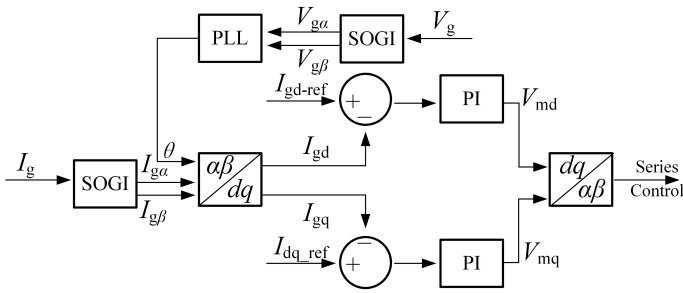


Fig. 3. Series injection control block diagram.

We recommend controlling each module independently to account for phase imbalances. Fig. 3 illustrates a grid-synchronous current control scheme for the fundamental frequency, where V_g is the grid voltage, and I_g is the grid current. Each module has its own dedicated control for managing phase asymmetries. For harmonics, the scheme is replicated at the respective frequencies. With the current control of floating modules, the open-loop control of the LLCs, and the voltage-current double loop control of AFE [14], the power flow between the AFE-LLC dc link and the floating-module dc link consequently emerges as a by-product.

III. FILTER ANALYSIS

The whole system can be installed on on-street utility boxes, as shown in Fig. 4. It replaces the conventional series inductor filter with the parasitic inductance of the three-phase cables. Since the inductorless system can operate at megahertz, the microhenry level parasitic inductance can satisfy the requirement. This section analyses the parasitic inductance of the system.

A. Parasitic inductance of the cabin model

As shown in Fig. 4, three-phase cables come out from the ground; one group of cables supplies the shunt grid interface (active front end + isolated dc/dc converter), while the other group go through the floating module and back to the ground, either to another grid or load.

The interior edge of each cable and the copper bar form a square loop, where the magnetic flux passes into and results in a loop inductance. This loop inductance can serve as filtering inductors, thus minimizing the ripple resulting from modulation. For simplicity, each loop is regarded as a rectangle and parallel to each other, with a length of l_1 (l_2 , l_3) and width of h_1 (h_2 , h_3); three rectangle loops are separated with Δl_{12} (Δl_{13} , Δl_{23}) and Δh_{12} (Δh_{13} , Δh_{23}); the copper bars are approximated as cylindrical cables, whose radius are the same as the grid cable r . The inductance matrix of the three-phase cabin model is

$$L_{\text{cabin}} = \begin{bmatrix} L_{11} & M_{12} & M_{13} \\ M_{12} & L_{22} & M_{23} \\ M_{13} & M_{23} & L_{33} \end{bmatrix} \quad (1)$$

where L_{11} , L_{22} , and L_{33} are self inductance of each phase and M_{12} , M_{13} , and M_{23} are mutual inductance.

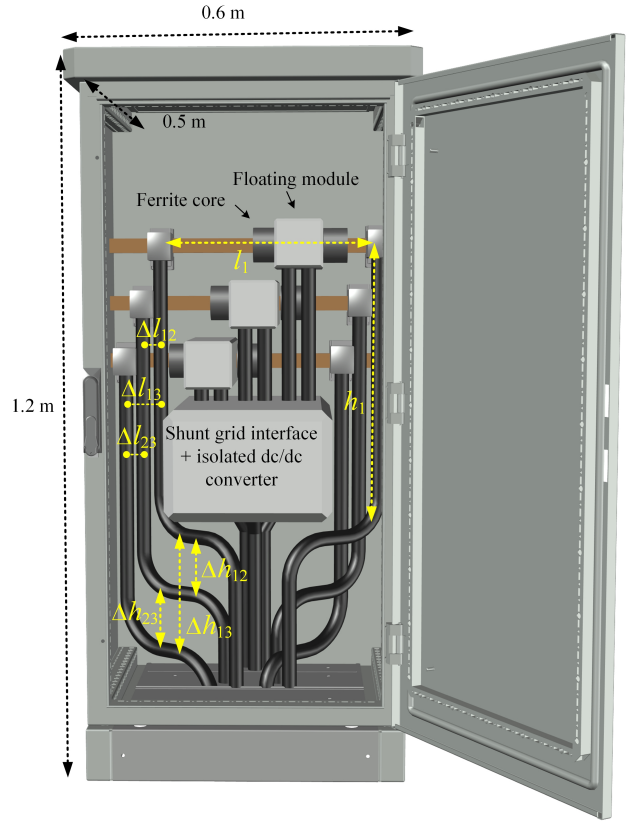


Fig. 4. Distribution grid cabinet model

The self-inductance of phase 1 can be derived as:

$$\begin{aligned} L_{11} &= \frac{\psi_{11}}{I_1} = \frac{2}{I_1} \times \frac{\mu_0 I_1}{2\pi x} \int_r^{l_1-r} \int_r^{h_1-r} dx dy \\ &+ \frac{2}{I_1} \times \frac{\mu_0 I_1}{2\pi x} \int_r^{h_1-r} \int_r^{l_1-r} dx dy \\ &= \frac{\mu_0}{\pi} (h_1 - 2r) \ln \left(\frac{l_1 - r}{r} \right) \\ &+ \frac{\mu_0}{\pi} (l_1 - 2r) \ln \left(\frac{h_1 - r}{r} \right) \end{aligned} \quad (2)$$

where ψ_{11} is the total magnetic flux through loop 1 due to itself; l_1 and h_1 are the length and width of loop 1, respectively; and I_1 is the phase 1 current.

The mutual inductance between phase 1 and phase 2 follows equation (3), obtained by dividing the total flux to loop 1 contributed by phase 2 by the current of phase 2. The upper segment and right segment produce part of the inverse flux and need to be deducted.

Similarly, the mutual inductance between phase 1 and phase 3 follows equation (4).

Supposing the three-phase currents are balanced, the equivalent phase inductance can be derived as:

$$\begin{bmatrix} L_1 \\ L_2 \\ L_3 \end{bmatrix} = \begin{bmatrix} L_{11} + M_{12} \cdot e^{j \cdot 2\pi/3} + M_{13} \cdot e^{j \cdot 4\pi/3} \\ M_{21} \cdot e^{j \cdot 2\pi/3} + L_{22} + M_{23} \cdot e^{j \cdot 4\pi/3} \\ M_{31} \cdot e^{j \cdot 2\pi/3} + M_{32} \cdot e^{j \cdot 4\pi/3} + L_{33} \end{bmatrix} \quad (5)$$

$$\begin{aligned}
M_{12} &= \frac{\psi_{12}}{I_2} = \frac{\mu_0}{2\pi x} \int_{r+\Delta l_{12}}^{l_2-r} \int_r^{h_2-\Delta h_{12}-r} dx dy + \frac{\mu_0}{2\pi x} \int_{r+\Delta h_{12}}^{h_2-r} \int_r^{l_2-\Delta l_{12}-r} dx dy + \frac{\mu_0}{2\pi x} \int_r^{h_2-\Delta h_{12}-r} \int_r^{l_2-\Delta l_{12}-r} dx dy \\
&+ \frac{\mu_0}{2\pi x} \int_r^{l_2-\Delta l_{12}-r} \int_r^{h_2-\Delta h_{12}-r} dx dy - \frac{\mu_0}{2\pi x} \int_r^{\Delta l_{12}-r} \int_r^{l_2-\Delta l_{12}-r} dx dy - \frac{\mu_0}{2\pi x} \int_r^{\Delta l_{12}-r} \int_r^{h_2-\Delta l_{12}-r} dx dy \\
&= \frac{\mu_0}{2\pi} (h_2 - \Delta h_{12} - 2r) \ln \left(\frac{l_2-r}{r+\Delta l_{12}} \frac{l_2-\Delta l_{12}-r}{r} \frac{r}{\Delta l_{12}-r} \right) + \frac{\mu_0}{2\pi} (l_2 - \Delta l_{12} - 2r) \ln \left(\frac{h_2-r}{r+\Delta l_{12}} \frac{h_2-\Delta h_{12}-r}{r} \frac{r}{\Delta h_{12}-r} \right)
\end{aligned} \tag{3}$$

$$M_{13} = \frac{\mu_0}{2\pi} (h_3 - \Delta h_{13} - 2r) \ln \left(\frac{l_3-r}{r+\Delta l_{13}} \frac{l_3-\Delta l_{13}-r}{r} \frac{r}{\Delta l_{13}-r} \right) + \frac{\mu_0}{2\pi} (l_3 - \Delta l_{13} - 2r) \ln \left(\frac{h_3-r}{r+\Delta l_{13}} \frac{h_3-\Delta h_{13}-r}{r} \frac{r}{\Delta h_{13}-r} \right) \tag{4}$$

Our domestic cabin model has following parameters: l_1, l_2, l_3 : 0.5 m; h_1, h_2, h_3 : 0.8 m; $\Delta l_{12}, \Delta l_{23}$: 0.1 m; Δl_{13} : 0.2 m; $\Delta h_{12}, \Delta h_{23}$: 0.2 m; Δh_{13} : 0.4 m; r : 0.0065 m. Putting these parameters into the equation (2)~(4), the parasitic inductance matrix is $L_{\text{cabin}} = \begin{bmatrix} 2.29 \mu\text{H} & 0.59 \mu\text{H} & 0.18 \mu\text{H} \\ 0.59 \mu\text{H} & 2.29 \mu\text{H} & 0.59 \mu\text{H} \\ 0.18 \mu\text{H} & 0.59 \mu\text{H} & 2.29 \mu\text{H} \end{bmatrix}$

Consequently, the real part of each phase inductance is around 2 μH .

B. Ripple analysis

Fig. 5 shows a simplified diagram of the voltage and current across the floating module via SPWM modulation. Based on that, the inductance can be derived along with the following equations:

$$V_{\text{module}} - V_{\text{dc}} = L \cdot \frac{\Delta i_{\text{pp}}}{\Delta t} \tag{6}$$

$$\Delta t = kT \tag{7}$$

$$V_{\text{module}} = k \cdot V_{\text{dc}} \tag{8}$$

$$k = m \cdot \sin(2\pi f_0 t) \tag{9}$$

where V_{module} is the voltage after filtering; V_{dc} is the voltage before filtering; k is the switch-on ratio; T is the switching period; f_0 is the fundamental frequency; and m is the modulation index.

By solving above equations, the current ripple can be expressed as

$$\Delta i_{\text{pp}} = \frac{V_{\text{dc}}}{2 \cdot L \cdot f_{\text{sw}}} \cdot (1 - m \cdot \sin(2\pi f_0 t)) \cdot m \cdot \sin(2\pi f_0 t) \tag{10}$$

By deriving the derivative of Δi_{pp} , the maximum current ripple $\Delta i_{\text{pp_max}}$ can be gotten: $V_{\text{dc}} / (8L \cdot f_{\text{sw}})$. For the case where V_{dc} is 48 V, L is 2 μH calculated above, and f_{sw} is 1 MHz, the maximum current ripple would be around 1.5 A.

IV. EXPERIMENTAL VALIDATION

We implement an experimental system to validate the basic functions: voltage adjustment and phase shift. For better presentation, we show the single-phase's experimental results in this section. A GaN floating module switching at 1 megahertz is direct-injected to a 230 V grid, and supplies the load: either a 1 mH and 66 Ω inductive load (for validating phase adjustment) or a 66 Ω resistive load (for validating voltage adjustment). The parasitic inductance of the system is measured to be 2 μH .

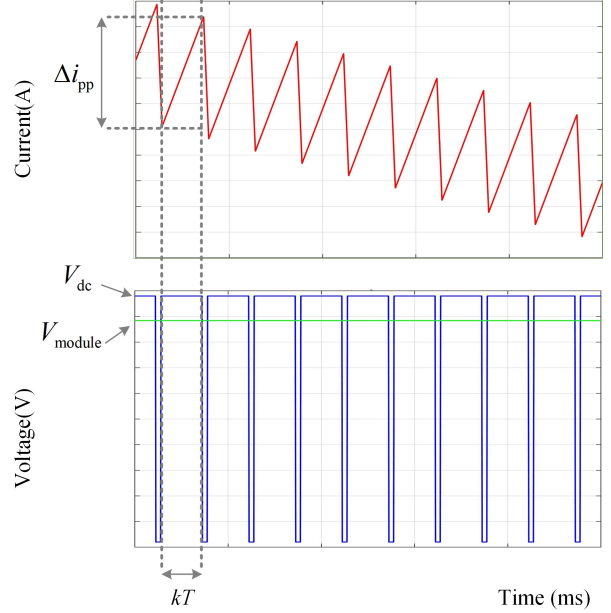


Fig. 5. Current and voltage of the floating module

A. Voltage adjustment

Fig. 6 exemplifies the capability of the floating module to modulate the grid voltage, either raising or lowering it. The circuit switches from the bypass state (denoted by the pink curve), where the current is allowed to pass through without modulation, to the modulation state, where a synchronous voltage is instantly introduced, raising the voltage (as illustrated by the shift from the blue curve to the green curve), which in turn boosts the line current (the yellow curve). Conversely, when a reversed voltage is applied, both the voltage and line current decrease. With its ability to adjust voltage, the system is able to effectively handle long or short-term rms fluctuations (surges, spikes, sags, swells, over-voltage, and under-voltage), and control power flow in the distribution grid.

B. Phase shift

The shifting of the grid voltage (the yellow curve) with respect to the original voltage (the blue curve) is depicted in Fig. 7. To compensate for the phase difference between the voltage and the current, the floating module (the light blue

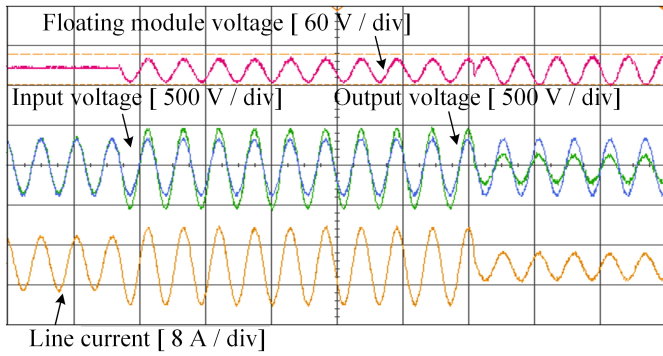


Fig. 6. Experimental results for voltage adjustment

curve) modulates to inject a synchronous voltage with a controlled phase displacement in series with the line. The phase shift function enables the system for harmonic compensation and power factor correction.

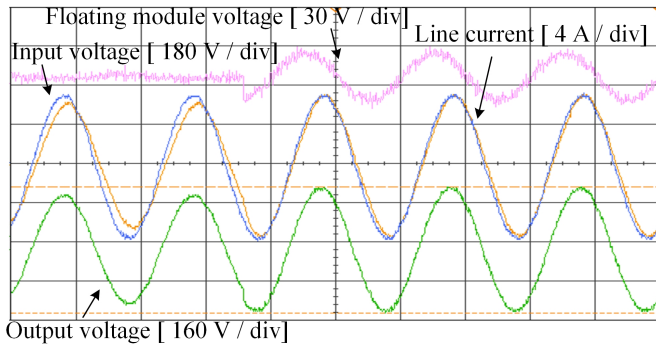


Fig. 7. Experimental results for phase shift

C. Zoomed floating module voltage

Fig. 8 displays the zoomed voltage waveform of the floating module in one cycle. Despite the absence of any series filtering inductor, the ripple ratio remains below 5%, benefiting from the microhenry-level parasitic inductance inherent in the proposed system.

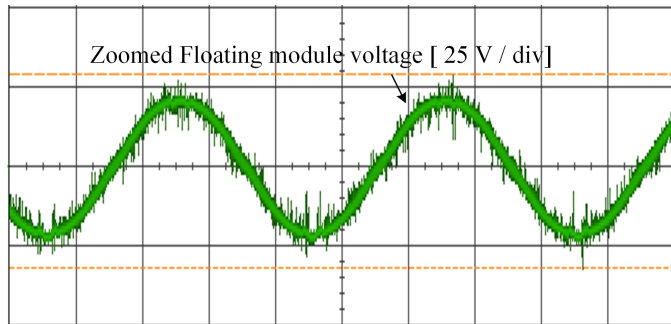


Fig. 8. Zoomed voltage waveform of the floating module

V. CONCLUSION

In the paper, we present a novel power control circuit consisting of high-current, low-voltage GaN modules that are phase potential floating, a shunt interface that operates with low-current and full voltage as the power source, such as an active front-end, and a high-frequency dc/dc converter for isolation and voltage conversion. The suggested approach gets rid of bulky transformers and has significant potential to be sufficiently compact for deployment on utility boxes located on the street, while also leveraging the benefits of parasitic impedance for filtering.

REFERENCES

- [1] E. Veldman and R. A. Verzijlbergh, "Distribution Grid Impacts of Smart Electric Vehicle Charging From Different Perspectives," in *IEEE Transactions on Smart Grid*, vol. 6, no. 1, pp. 333-342, Jan. 2015.
- [2] M. S. H. Nizami, M. J. Hossain and K. Mahmud, "A Coordinated Electric Vehicle Management System for Grid-Support Services in Residential Networks," in *IEEE Systems Journal*, vol. 15, no. 2, pp. 2066-2077, June 2021.
- [3] M. A. Khan, A. Haque and V. S. B. Kurukuru, "Dynamic Voltage Support for Low-Voltage Ride-Through Operation in Single-Phase Grid-Connected Photovoltaic Systems," in *IEEE Transactions on Power Electronics*, vol. 36, no. 10, pp. 12102-12111, Oct. 2021.
- [4] T. Aziz and N. Ketjoy, "PV Penetration Limits in Low Voltage Networks and Voltage Variations," in *IEEE Access*, vol. 5, pp. 16784-16792, 2017.
- [5] X. Jiang, Y. Zhou, W. Ming, P. Yang and J. Wu, "An Overview of Soft Open Points in Electricity Distribution Networks," in *IEEE Transactions on Smart Grid*, vol. 13, no. 3, pp. 1899-1910, May 2022.
- [6] L. Gyugyi, C. D. Schauder, S. L. Williams, T. R. Rietman, D. R. Torgerson and A. Edris, "The unified power flow controller: a new approach to power transmission control," in *IEEE Transactions on Power Delivery*, vol. 10, no. 2, pp. 1085-1097, April 1995.
- [7] X. Zhao et al., "Multimode Operation Mechanism Analysis and Power Flow Flexible Control of a New Type of Electric Energy Router for Low-Voltage Distribution Network," in *IEEE Transactions on Smart Grid*, vol. 13, no. 5, pp. 3594-3606, Sept. 2022.
- [8] V. Khadkikar, "Enhancing Electric Power Quality Using UPQC: A Comprehensive Overview," in *IEEE Transactions on Power Electronics*, vol. 27, no. 5, pp. 2284-2297, May 2012.
- [9] M. Lu and S. M. Goetz, "A Highly Compact Transformerless Universal Power-Flow and Quality Control as well as Soft Open Point Circuit," *IECON 2022 – 48th Annual Conference of the IEEE Industrial Electronics Society*, Brussels, Belgium, 2022, pp. 1-6.
- [10] Wanyu Cao, Jianzhong Wu, Nick Jenkins, Chengshan Wang, Timothy Green, Operating principle of Soft Open Points for electrical distribution network operation, *Applied Energy*, Volume 164, 2016, Pages 245-257, ISSN 0306-2619.
- [11] J. Fang, F. Blaabjerg, S. Liu and S. M. Goetz, "A Review of Multilevel Converters With Parallel Connectivity," in *IEEE Transactions on Power Electronics*, vol. 36, no. 11, pp. 12468-12489, Nov. 2021.
- [12] S. M. Goetz, Z. Li, X. Liang, C. Zhang, S. M. Lukic and A. V. Peterchev, "Control of Modular Multilevel Converter With Parallel Connectivity—Application to Battery Systems," in *IEEE Transactions on Power Electronics*, vol. 32, no. 11, pp. 8381-8392, Nov. 2017.
- [13] M. Lu and S. M. Goetz, "Highly Compact Transformerless Universal Power-Flow and Quality Control Circuit," 2022 IEEE 1st Industrial Electronics Society Annual On-Line Conference (ONCON), Kharagpur, India, 2022, pp. 1-7.
- [14] J. R. Rodriguez, J. W. Dixon, J. R. Espinoza, J. Pontt and P. Lezana, "PWM regenerative rectifiers: state of the art," in *IEEE Transactions on Industrial Electronics*, vol. 52, no. 1, pp. 5-22, Feb. 2005.